

Forbidden dark matter assisted by first-order phase transition and associated gravitational waves

Satyabrata Mahapatra^{ID},^a **Partha Kumar Paul**^{ID},^b and **Narendra Sahu**^{ID}^b

^aSchool of Physical Sciences, Indian Institute of Technology Goa, Ponda-403401, Goa, India

^bDepartment of Physics, Indian Institute of Technology Hyderabad, Kandi, Telangana-502285, India.

E-mail: satyabrata@iitgoa.ac.in, ph22resch11012@iith.ac.in, nsahu@phy.iith.ac.in

Abstract. We propose a simple yet testable framework for light fermion dark matter (DM) with mass in the MeV–GeV range, charged under a dark $U(1)_D$ gauge symmetry. The $U(1)_D$ is spontaneously broken by a scalar field Φ , giving mass to the dark gauge boson X_D . The dominant DM annihilation proceeds via a forbidden channel, where the DM pair annihilates into slightly heavier dark gauge bosons and scalars after the dark-sector phase transition. Once the dark-sector phase transition occurs, the induced mass gap activates the forbidden annihilation channel, which in turn determines the DM relic abundance and naturally suppresses late-time annihilation. As a result, the scenario avoids stringent cosmic microwave background and indirect detection constraints that typically exclude thermal light DM. Moreover, the same symmetry-breaking phase transition is strongly first-order, producing a stochastic gravitational wave background that could be probed by upcoming space-based interferometers and pulsar timing arrays. We demonstrate that achieving the observed DM abundance tightly correlates the DM mass with the nucleation temperature of the phase transition. Thus, this setup links the DM relic abundance, dark-sector dynamics, and gravitational wave signals, offering complementary paths for discovery in both terrestrial and cosmological observations.

Contents

1	Introduction	1
2	Forbidden dark matter	3
3	The minimal model	3
4	First-order phase transition	5
5	Forbidden dark matter from first-order phase transition	6
6	Other relevant constraints	9
6.1	BBN constraint from Φ decay	9
6.2	Constraint from Higgs invisible decay	10
7	Gravitational wave from first-order phase transition	11
8	Conclusions	12
A	SM Higgs and Φ mixing	13
B	DM annihilation and scattering cross-sections	13
C	Details of first-order phase transition	14
D	Gravitational waves	15

1 Introduction

Understanding the identity of the dark matter (DM), which constitutes approximately 85% of the matter content of the Universe, remains one of the foremost challenges in modern cosmology. Robust gravitational evidence from galaxy rotation curves, gravitational lensing, and cluster dynamics [1–3], together with precision measurements of the cosmic microwave background (CMB) [4, 5], indicate that roughly a quarter of the total energy density of the Universe is composed of non-luminous and non-baryonic matter, whose microscopic nature remains unknown.

For several decades, Weakly Interacting Massive Particles (WIMPs) were regarded as the leading DM candidate, motivated by their natural appearance in many extensions of the Standard Model (SM) and their ability to reproduce the observed relic abundance via thermal freeze-out. However, as increasingly sensitive direct detection experiments have continued to report null results, the viability of the canonical WIMP paradigm has been placed under growing tension [6, 7]. In particular, the absence of statistically significant signals across multiple generations of direct detection experiments has led to increasingly stringent exclusion limits on WIMP–nucleon scattering cross sections. This mounting experimental pressure has motivated the exploration of alternative DM candidates, including light DM with masses $m_{\text{DM}} \lesssim 10$ GeV [8–18]. Such sub-GeV to GeV candidates are now being actively probed by a new generation of low-threshold experiments (e.g. SuperCDMS, SENSEI,

CRESST, DarkSide, DAMIC), which search for nuclear or electron recoils induced by light DM scattering [19–26].

However, even light DM produced via conventional thermal freeze-out is subject to severe cosmological and astrophysical constraints. For DM masses below the electroweak scale, thermal freeze-out generically implies sizable annihilation rates that persist well after chemical decoupling. Such late-time annihilations inject energy into the primordial plasma and are therefore tightly constrained by observations of the CMB as well as by indirect detection experiments [27]. In particular, CMB measurements strongly limit energy injection during the epoch of recombination, excluding standard s -wave annihilating DM with masses $m_{\text{DM}} \lesssim \mathcal{O}(10)\text{GeV}$ for visible final states [4, 27]. Complementary constraints arise from indirect searches for annihilation products in gamma rays and cosmic rays, such as those performed by Fermi-LAT and AMS-02, which rule out the canonical thermal annihilation cross section for DM masses below $\sim 20\text{ GeV}$ [28, 29]. Taken together, these results effectively exclude the simplest realizations of light thermal DM.

A viable alternative is the forbidden DM scenarios [30], wherein the dominant annihilation channel is kinematically suppressed at late times. In a forbidden model, DM annihilates into slightly heavier states during freeze-out, so that annihilation shuts off exponentially as the temperature drops, evading CMB bounds [30, 31]. For instance, one can arrange DM to annihilate into heavier dark-sector bosons or scalars, rather than directly into SM particles. However, if the final states are SM fields, the DM mass and couplings remain highly constrained by laboratory and astrophysical limits. We therefore consider a secluded dark sector in which the DM χ annihilates primarily into a dark gauge boson X_D and a dark Higgs scalar ϕ (which breaks the dark $U(1)$ symmetry). This hidden-sector forbidden annihilation can yield the correct relic density while allowing sizable DM–SM couplings (via gauge kinetic mixing or other portals) that keep the model phenomenologically accessible.

A key feature of this framework is that the forbidden channel only becomes viable after the dark gauge symmetry is broken. Before the phase transition, X_D and ϕ are effectively massless and would over-deplete the DM if couplings are large. Moreover, the sizable coupling needed to achieve the required relic density and make the DM observable tends to drive the dark-sector transition to be strongly first-order. Such a first-order phase transition produces a stochastic gravitational wave (GW) background that lies within the sensitivity of present and future GW detectors [32–35]. Thus, the model links DM freeze-out to gravitational wave cosmology: the same symmetry-breaking transition that enables forbidden annihilations also generates a potentially detectable GW signal. After symmetry breaking, the dark gauge boson and scalar acquire masses, and by tuning the mass splitting $(M_{X_D} + M_{\phi}) - (2M_{\chi})$ we can obtain the observed relic abundance while ensuring annihilations effectively shut off at late times, thereby evading the CMB and indirect detection constraints. In summary, this dark sector forbidden-DM scenario not only achieves the correct thermal relic density, but also offers multiple experimental avenues, including direct detection of DM, search for new forces, as well as gravitational wave astronomy. Moreover, the model predicts a striking correlation between the DM mass and the gravitational wave spectrum: heavier DM requires a higher-scale phase transition to maintain the forbidden mechanism, shifting the GW peak frequency to higher values. This robust model prediction provides a powerful consistency check, linking the microscopic properties of DM to distinct signatures in gravitational wave detectors.

The rest of the paper is built up as follows. In section 2, we discuss the forbidden DM. The minimal model is introduced in section 3, followed by the First-order phase transition,

which is discussed in section 4. We discuss the forbidden DM from the first-order phase transition in section 5. We discuss other phenomenological constraints in section 6. Section 7 discusses gravitational wave production from the first-order phase transition. We finally conclude in section 8.

2 Forbidden dark matter

We consider a scenario where a Dirac fermionic DM χ couples to dark sector states \mathcal{D}_1 and \mathcal{D}_2 , through an effective interaction term $\mathcal{L}_{\text{int}} \supset g_{\text{eff}} \bar{\chi} \chi \mathcal{D}_1 \mathcal{D}_2$. The relic abundance is determined through the annihilation process $\chi \bar{\chi} \rightarrow \mathcal{D}_1 \mathcal{D}_2$, with a thermally averaged cross-section of the order $\langle \sigma v \rangle \sim g_{\text{eff}}^4 / M_\chi^2$, where we assume that \mathcal{D}_1 and \mathcal{D}_2 are massless or negligible mass compared to χ . This can reproduce the observed DM abundance for weak-scale masses and a sizable coupling. For lighter DM below the weak scale, however, the annihilation cross-section becomes too large, driving the relic density to under-abundant values unless $g_{\text{eff}} \ll 1$. An attractive alternative is to consider annihilation into slightly heavier final states, the so-called forbidden channels. In this case, the annihilation is kinematically forbidden at zero temperature but proceeds in the early Universe thanks to the Boltzmann tail, leading to an exponentially suppressed cross-section at late times. This allows light DM to achieve the correct relic density even with order-one couplings [30, 31].

In the forbidden regime, the thermally averaged annihilation cross-section can be related to the reverse process by detailed balance,

$$\langle \sigma_{\chi \bar{\chi} \rightarrow \mathcal{D}_1 \mathcal{D}_2} v \rangle = \frac{n_{\mathcal{D}_1}^{\text{eq}} n_{\mathcal{D}_2}^{\text{eq}}}{(n_\chi^{\text{eq}})^2} \langle \sigma_{\mathcal{D}_1 \mathcal{D}_2 \rightarrow \chi \bar{\chi}} v \rangle, \quad (2.1)$$

where n_i^{eq} denotes the equilibrium number density of species i , which for non-relativistic particles is given by $n_i^{\text{eq}} = g_i (M_i T / 2\pi)^{3/2} e^{-M_i / T}$. Defining $r_i = M_{\mathcal{D}_i} / M_\chi$, $\Delta = M_{\mathcal{D}_1} + M_{\mathcal{D}_2} - 2M_\chi$ and $x = M_\chi / T$, the ratio of equilibrium densities yield,

$$\frac{n_{\mathcal{D}_1}^{\text{eq}} n_{\mathcal{D}_2}^{\text{eq}}}{(n_\chi^{\text{eq}})^2} \simeq \frac{g_{\mathcal{D}_1} g_{\mathcal{D}_2}}{g_\chi^2} (r_1 r_2)^{3/2} e^{-2\Delta x}$$

where the exponential factor $e^{-2\Delta x}$ encodes the kinematic suppression from the heavier final states. Including the phase-space factor for the reverse process, the thermally averaged forbidden annihilation cross-section can be written schematically as

$$\langle \sigma_{\chi \bar{\chi} \rightarrow \mathcal{D}_1 \mathcal{D}_2} v \rangle = \frac{g_{\mathcal{D}_1} g_{\mathcal{D}_2}}{g_\chi^2} \mathcal{F}(r_1, r_2) e^{-2\Delta x} \langle \sigma_{\mathcal{D}_1 \mathcal{D}_2 \rightarrow \chi \bar{\chi}} v \rangle, \quad (2.2)$$

where $\mathcal{F}(r_1, r_2)$ is a kinematic function, which for nearly degenerate final states $M_{\mathcal{D}_1} \simeq M_{\mathcal{D}_2}$, reduces to the familiar $(1 + \Delta)^{3/2}$ factor in the literature. The key point is that the annihilation rate is exponentially suppressed, so that the resulting relic abundance scales approximately as $\Omega_\chi h^2 \propto e^{2\Delta x_f}$ with $x_f = M_\chi / T_f$, the freeze-out parameter. As a result, even relatively light DM with sizable couplings can reproduce the observed relic density by appropriately tuning the mass splitting Δ .

3 The minimal model

We now introduce a minimal setup that realizes the forbidden DM scenario triggered by a first-order phase transition in the dark sector. The model contains a Dirac fermion χ with

charge +1 under a $U(1)_D$ gauge symmetry and a complex scalar singlet $\Phi = (\phi + i\eta)/\sqrt{2}$ with charge -1. The relevant dark sector Lagrangian is given by

$$\mathcal{L}_{U(1)_D} = \bar{\chi}(i\gamma^\mu \mathcal{D}_\mu - M_\chi)\chi - \frac{1}{4}X_{\mu\nu}X^{\mu\nu} - \frac{\epsilon}{2}B_{\mu\nu}X^{\mu\nu} + (\mathcal{D}_\mu\Phi)^*(\mathcal{D}_\mu\Phi) + \mu_\Phi^2\Phi^*\Phi - \lambda_\Phi(\Phi^*\Phi)^2, \quad (3.1)$$

where the covariant derivative is defined as $\mathcal{D}_\mu = \partial_\mu + iQ_D g_D(X_D)_\mu$ with Q_D being the charge of the particle under $U(1)_D$ symmetry, ϵ is the kinetic mixing parameter between the dark gauge field X_μ and the hypercharge gauge boson B_μ . After spontaneous breaking of the $U(1)_D$ symmetry, the scalar can be parameterized around its vacuum expectation value (vev) as

$$\Phi = \frac{\phi + v_\phi}{\sqrt{2}}, \quad (3.2)$$

where v_ϕ denotes the vev of the dark scalar field. The symmetry breaking generates masses for the dark gauge boson and the physical scalar ϕ as

$$M_{X_D} = g_D v_\phi, \quad M_\phi = \sqrt{2\lambda_\Phi} v_\phi. \quad (3.3)$$

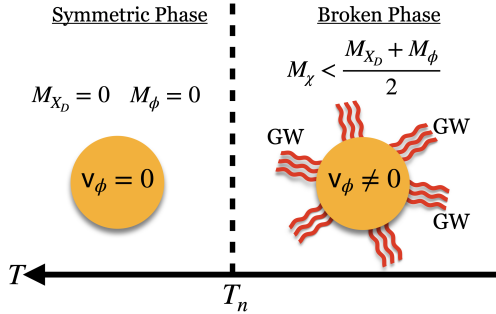


Figure 1: Pictorial representation of our model, which gives rise to gravitational waves via a first-order phase transition and correct relic of DM through the forbidden channel.

A pictorial summary of the scenario proposed is shown in Fig. 1, which summarizes the essential thermal history of the dark sector in this framework. In the high-temperature symmetric phase, the dark scalar field sits at the origin, $v_\phi = 0$, so that both the dark gauge boson and the scalar remain massless and the forbidden annihilation channel is not operative. As the temperature drops below the nucleation temperature T_n , the dark sector undergoes a first-order phase transition, and the scalar acquires a non-zero vacuum expectation value, $v_\phi \neq 0$, thereby generating masses for both the dark gauge boson and the scalar itself.

In the broken phase, the mass hierarchy is arranged such that $M_\chi < (M_{X_D} + M_\phi)/2$, rendering the process $\chi\bar{\chi} \rightarrow X_D\phi$ a forbidden channel at late times while still allowing it to proceed efficiently in the early Universe due to the thermal population of the heavier final states. This realizes the forbidden DM mechanism discussed above and enables the correct relic abundance for light DM with sizable couplings while simultaneously producing a stochastic gravitational wave background from the strong first-order phase transition. Taken together, this setup tightly links the origin of the DM relic density to testable signals in upcoming gravitational wave experiments and dark sector searches. Prior to analyzing the DM phenomenology, we first outline the dynamics of the dark sector phase transition and determine the regions of parameter space that yield a strongly first-order transition.

4 First-order phase transition

As emphasized above, the same dark sector dynamics that generate the correct relic abundance through a forbidden channel is facilitated by a strong first-order phase transition, providing a complementary source of a stochastic gravitational wave background. In this section, we focus on the thermal evolution of the scalar field and identify the regions of parameter space in which the symmetry breaking of $U(1)_D$ proceeds via a strongly first-order phase transition, suitable for generating potentially observable gravitational wave signals.

The scalar potential gets thermal corrections at finite temperature, and it can be written as

$$V_{\text{eff}}(\phi, T) = V_{\text{tree}}(\phi) + V_{\text{CW}}(\phi) + V_{\text{ct}}(\phi) + V_T(\phi, T) + V_{\text{daisy}}(\phi, T), \quad (4.1)$$

where $V_{\text{tree}}(\phi)$ is the tree level potential, $V_{\text{CW}}(\phi)$ is the Coleman-Weinberg one-loop correction, $V_{\text{ct}}(\phi)$ is the counter term, $V_T(\phi)$ is the finite temperature contribution, and V_{daisy} accounts for the daisy correction. The explicit expressions of these terms are given in Appendix C. At high temperature, the effective potential is minimized at $\phi = 0$. As the Universe cools and the temperature drops, the shape of the potential evolves, and a second, energetically favorable minimum at $\phi \neq 0$ can appear, separated from the origin by a potential barrier. In this situation, the system undergoes a first-order phase transition (FOPT), in which bubbles of the true vacuum nucleate within the metastable false vacuum and subsequently expand.

Such an FOPT can efficiently produce gravitational waves via three main processes: bubble wall collisions, sound waves in the plasma, and magnetohydrodynamic turbulence in the plasma. The corresponding spectra and their combination into the total gravitational wave signal are discussed in detail in Appendix D. For phenomenological purposes, the gravitational wave signal is largely characterized by two key parameters evaluated at the nucleation temperature T_n : the strength of the transition, quantified by the ratio of the released vacuum energy to the radiation energy density, and the inverse duration of the transition in units of the Hubble rate. These are conventionally expressed as

$$\alpha(T_n) = \frac{\rho_{\text{vac}}(T_n)}{\rho_{\text{rad}}(T_n)}, \quad (4.2)$$

where

$$\rho_{\text{vac}}(T) = V_{\text{eff}}(\phi_{\text{false}}, T) - V_{\text{eff}}(\phi_{\text{true}}, T) - T \frac{\partial}{\partial T} [V_{\text{eff}}(\phi_{\text{false}}, T) - V_{\text{eff}}(\phi_{\text{true}}, T)], \quad (4.3)$$

and

$$\rho_{\text{rad}}(T) = \frac{\pi^2}{30} g_* T^4, \quad (4.4)$$

with g_* denoting the number of relativistic degrees of freedom (d.o.f) at $T = T_n$. The parameter $\alpha(T_n)$ thus measures how strongly the phase transition energy budget departs from that of a purely radiation-dominated Universe. The timescale of the transition is encoded in the quantity β , defined as the inverse duration of the phase transition and commonly expressed in units of the Hubble rate at nucleation,

$$\frac{\beta}{\mathcal{H}(T_n)} \simeq T_n \frac{d}{dT} \left(\frac{S_3}{T} \right) \Big|_{T=T_n}. \quad (4.5)$$

where S_3 is the three-dimensional Euclidean action of the critical bubble configuration. A smaller value of $\beta/\mathcal{H}(T_n)$ corresponds to a slower, more prolonged transition and typically enhances the gravitational wave signal, while larger values indicate a faster transition with a more suppressed signal.

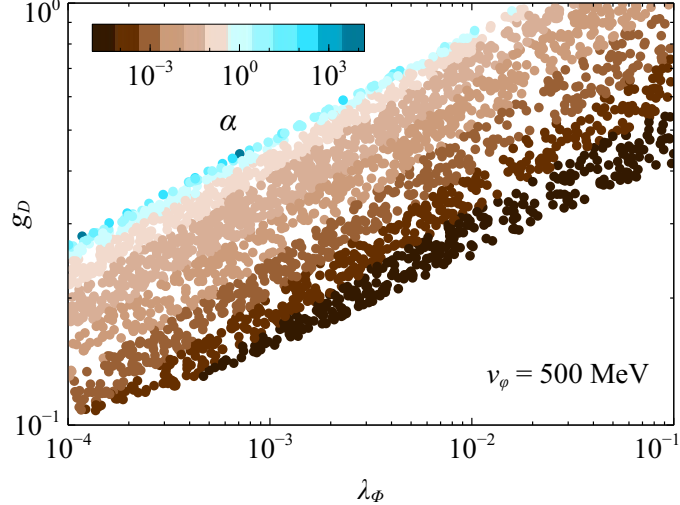


Figure 2: Allowed regions in the dark sector gauge coupling (g_D) vs scalar self-coupling (λ_ϕ) plane for a fixed scalar vev $v_\phi = 500$ MeV with the color scale representing the strength of the first-order phase transition (quantified by α), with larger values indicating stronger transitions.

In Fig. 2 we show the region of parameter space in the g_D – λ_ϕ plane that leads to a first-order phase transition for a fixed dark scalar vev $v_\phi = 500$ MeV. The color code indicates the corresponding value of $\alpha(T_n)$, providing a measure of the transition strength. This plot highlights the range of gauge and scalar couplings for which the dark sector undergoes a sufficiently strong FOPT to generate potentially detectable gravitational waves.

5 Forbidden dark matter from first-order phase transition

Having identified regions of the dark sector parameter space where the $U(1)_D$ symmetry breaking proceeds via a strong first-order phase transition, we now turn to the DM phenomenology of the same setup. In particular, we analyze how the phase transition reshapes the available annihilation channels and enables the forbidden process to control the relic abundance of χ .

In our setup, three annihilation channels can in principle contribute to setting the DM abundance:

$$\bar{\chi}\chi \rightarrow X_D X_D, \quad \bar{\chi}\chi \rightarrow X_D \phi, \quad \bar{\chi}\chi \rightarrow \bar{f}f, \quad (5.1)$$

where f denotes SM fermions. The process $\bar{\chi}\chi \rightarrow \bar{f}f$ is induced by the kinetic mixing between the dark gauge boson X_D and the hypercharge gauge boson, but its contribution to the relic density can be made negligible by taking the kinetic mixing parameter ϵ sufficiently small. In this regime, the DM abundance is primarily determined by annihilations into dark-sector states.

As discussed in Sec. 4, and evident from Fig. 2, a strong first-order phase transition in the dark sector is obtained for $g_D \gg \lambda_\Phi$, which implies $M_{X_D} \gg M_\phi$ at fixed v_ϕ . Consequently, the phase-space suppression for $\bar{\chi}\chi \rightarrow X_D X_D$ is more severe than for the mixed final state $\bar{\chi}\chi \rightarrow X_D \phi$, so that the latter process typically dominates the annihilation rate in the broken phase. Thus, to realize the forbidden DM mechanism, we focus on the region of parameter space where

$$2M_\chi < M_{X_D} + M_\phi, \quad (5.2)$$

so that $\bar{\chi}\chi \rightarrow X_D \phi$ is kinematically forbidden for non-relativistic DM at zero temperature, but becomes active in the early Universe thanks to the high energy tail of the thermal distribution, which allows the production of the heavier final states. In this regime, the relic abundance of χ is determined by the freeze-out of the forbidden channel after the dark sector phase transition. The DM yield $Y_\chi \equiv n_\chi/s$ evolves according to the Boltzmann equation

$$\frac{dY_\chi}{dx} = -\frac{sx}{\mathcal{H}(M_\chi)} \langle \sigma v \rangle_{\bar{\chi}\chi \rightarrow X_D \phi} \left(Y_\chi^2 - (Y_\chi^{eq})^2 \right) \quad (5.3)$$

where $x = M_\chi/T$ is the dimensionless parameter to track the evolution of temperature, Y_χ^{eq} is the equilibrium abundance of χ *i.e.* $Y_\chi^{eq} = 0.116 \frac{g_\chi}{g_*} x^2 K_2(x)$, g_* is the effective number of relativistic d.o.f at temperature T , $K_2(x)$ is the modified Bessel function of second kind. The Hubble parameter and entropy density can be written as $\mathcal{H}(M_\chi) = 1.66 \sqrt{g_*} \frac{M_\chi^2}{M_{Pl}}$, $s = \frac{2\pi^2}{45} g_* M_\chi^3 x^{-3}$, where $M_{Pl} = 1.22 \times 10^{19}$ GeV is the Planck mass. Solving the Boltzmann equation yields the late-time value of Y_χ , from which the present relic abundance follows as

$$\Omega_{DM} h^2 \simeq 0.118 \left(\frac{Y_\chi}{4.2 \times 10^{-10}} \right) \left(\frac{M_\chi}{1 \text{ GeV}} \right). \quad (5.4)$$

In the *left* panel of Fig. 3, we show the DM relic abundance as a function of $\Delta =$

Table 1: Benchmark points for satisfying correct DM relic via forbidden channel, and observable gravitational wave from first-order phase transition

BP _s	M_χ (MeV)	M_{X_D} (MeV)	M_ϕ (MeV)	λ_Φ	v_ϕ (MeV)	g_D	T_c (MeV)	T_n (MeV)	α_*	β_*/\mathcal{H}_*
BP1	31.77	77.711	11.7853	0.006945	100	0.77711	25.2707	6.91296	7.88957	141.354
BP2	71.623	188.326	14.06	0.0003955	500	0.37665	60.4405	11.2753	40.6705	1947.2
BP3	351.612	812.94	129.297	0.00823	1000	0.81294	266.225	87.034	2.6914	169.2208
BP4	6130	12795.46	1852.74	0.004291	20000	0.63977	4824.76	2924.80	0.05421	950.132

$(M_{X_D} + M_\phi - 2M_\chi)/2M_\chi$ for the four benchmark points listed in Table 1. Since the thermally averaged cross-section for a forbidden channel is exponentially suppressed, $\langle \sigma v \rangle \propto e^{-2\Delta x_f}$, the relic abundance approximately scales as $\Omega_{DM} h^2 \propto e^{2\Delta x_f}$, and thus increases with Δ . For each benchmark, the observed relic density is obtained at a particular value of $\Delta > 0$, namely $\Delta = 0.408, 0.413, 0.34$, and 0.195 for BP1–BP4, respectively. The *right* panel of Fig. 3 illustrates the evolution of the DM yield for BP2. The blue dashed curve shows the equilibrium abundance, and the blue solid curve shows the actual yield when the forbidden channel governs freeze-out after the dark sector phase transition. The red curve corresponds to the hypothetical case without the phase transition, in which X_D and ϕ remain massless, and the same coupling leads to an unsuppressed, allowed annihilation channel, resulting in a strongly under-abundant relic.

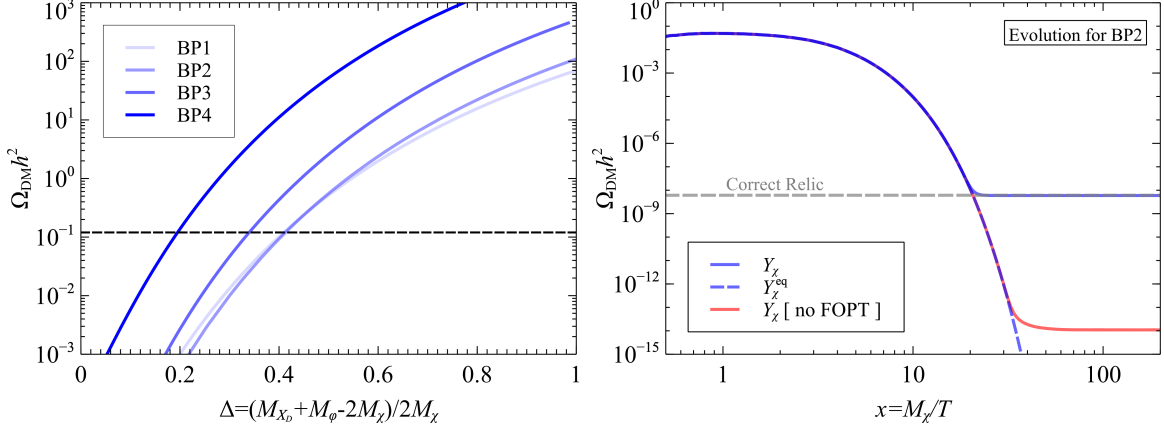


Figure 3: *Left:* Dark matter relic density $\Omega_{\text{DM}} h^2$ as a function of Δ for the benchmark points in Table 1. *Right:* Evolution of the dark matter yield for *BP2*. The blue dashed line shows the equilibrium yield, while the blue solid line shows the actual yield when the relic abundance is set by the freeze-out of the forbidden process $\chi\bar{\chi} \rightarrow X_D\phi$ after the dark sector phase transition. The red solid line illustrates the under-abundant relic that would result for *BP2* in the absence of the phase transition, where the same channel proceeds with effectively massless final-state particles.

In Fig. 4, we present the viable parameter space in the ϵ - Δ plane for *BP1*, *BP2*, *BP3*, and *BP4* (top left, top right, bottom left, and bottom right, respectively), as defined in Table 1. For each benchmark, the shaded and hatched regions summarize current constraints from DM-electron and DM-nucleon scattering experiments, as well as bounds from accelerator and astrophysical probes, while the vertical black dashed line indicates the value of Δ that reproduces the observed relic abundance. The light blue region corresponds to parameter choices where χ fails to maintain kinetic equilibrium with the SM bath, primarily determined by the t -channel process $\chi e^- \rightarrow \chi e^-$. The region above the red solid curve satisfies $\Gamma_{\chi\bar{\chi} \rightarrow e^+e^-} / H \gtrsim 1$ at $x = 10$, implying that annihilations into e^+e^- substantially modify the relic density and the simple forbidden-channel picture no longer applies. The dark red band near $\epsilon \sim 10^{-11}$ is excluded by big bang nucleosynthesis (BBN) considerations, since in this regime the dark gauge boson X_D becomes too long-lived and disrupts standard nucleosynthesis.

Limits from DM- e scattering experiments DS-LM [36], DS-50 [37], XENON1T [19], and PandaX-4T [23] are shown in the green, pink-hatched, yellow, and pink shaded regions. Direct-detection limits from DM-nucleon experiments DS-50 [38], SuperCDMS [39], and DS-LM [36] are indicated by the cyan-green solid, cyan dashed, and blue dotted lines. Additional constraints from NA64 [40] (light blue hatched), BaBar [41] (dark blue hatched), and SN1987A [42] (light orange hatched) are included as well. Similar features and trends are visible across all four benchmark panels, illustrating that the interplay between relic-density requirements, kinetic equilibrium, and the various experimental and cosmological bounds consistently carves out a narrow but well-defined region in ϵ - Δ space where the forbidden DM scenario remains viable.

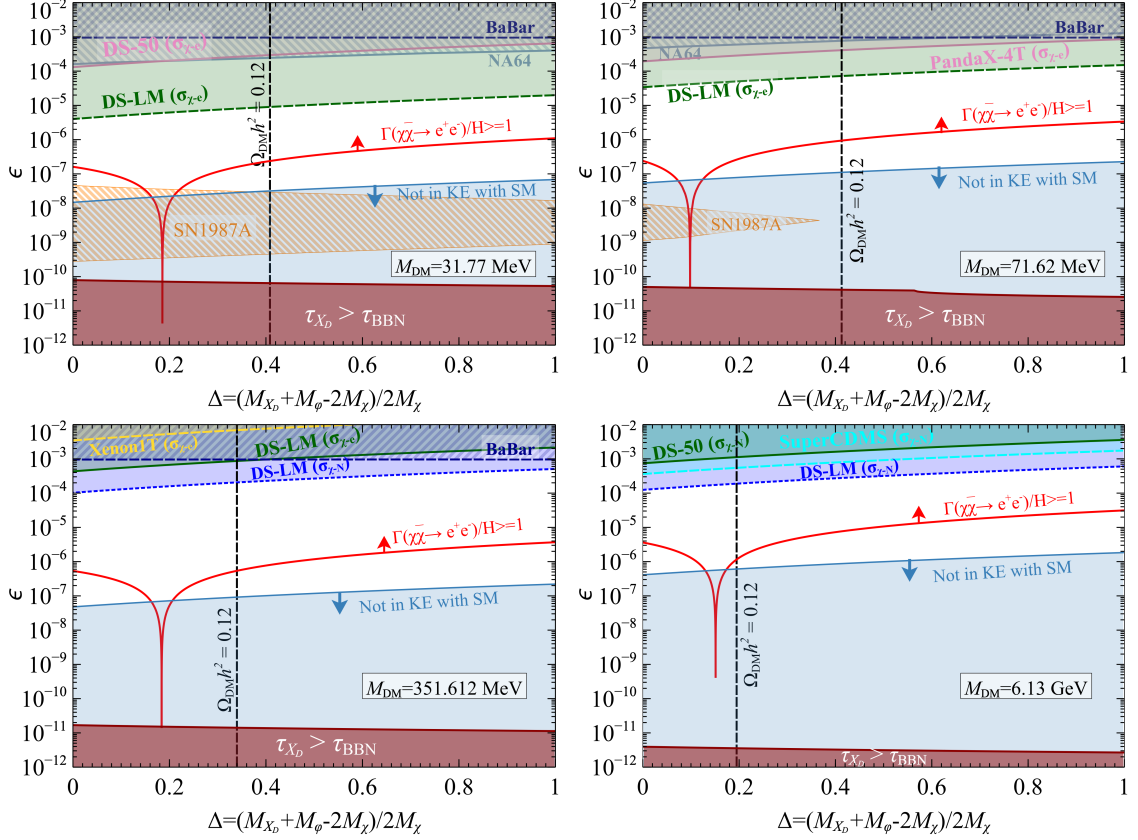


Figure 4: Parameter space in the ϵ – Δ plane for $BP1$, $BP2$, $BP3$, and $BP4$ (top left, top right, bottom left, bottom right respectively), as defined in Table 1. Shaded and hatched regions indicate different possible constraints; the vertical black dashed line shows the value of Δ yielding the correct dark matter relic abundance for each benchmark.

6 Other relevant constraints

In addition to relic-density, direct-detection, and other requirements discussed in the previous section, the scenario is subject to several cosmological and collider bounds that further shape the viable parameter space. In this section, we discuss the limits from BBN on the lifetime of the scalar ϕ , and bounds on invisible Higgs decays from LHC measurements.

6.1 BBN constraint from Φ decay

The light scalar, ϕ , can decay into the SM fermions after mixing with the SM Higgs boson. The partial decay width into a fermion pair is given as

$$\Gamma_{\phi \rightarrow ff} = \sin^2 \theta \left(\frac{m_f}{v_0} \right)^2 \frac{M_\phi}{8\pi} \left(1 - \frac{4m_f^2}{M_\phi^2} \right)^{\frac{3}{2}}, \quad (6.1)$$

where m_f is the mass of the fermion, $\sin \theta$ is the mixing angle between the SM Higgs and scalar ϕ , v_0 is the vev of SM Higgs. The corresponding lifetime is given by

$$\tau_\phi = (\Gamma_{\phi \rightarrow ff})^{-1}. \quad (6.2)$$

The singlet scalar must decay before the onset of BBN; otherwise, its late-time decay would disrupt the successful predictions of primordial nucleosynthesis.

6.2 Constraint from Higgs invisible decay

If the dark sector particles X_D and ϕ are lighter than $M_h/2$, the SM Higgs boson can decay into pairs of these particles, contributing to its invisible decay width. Recent LHC measurements constrain the invisible branching ratio to $\mathcal{Br}(h \rightarrow \text{inv}) \leq 0.145$ [43]. The

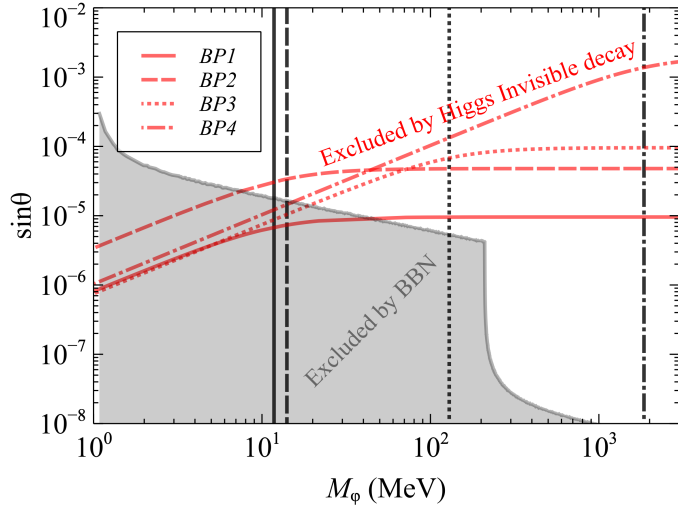


Figure 5: Allowed parameter space from BBN and Higgs invisible decay constraints in the $\sin \theta$ - M_ϕ plane. The gray shaded region is excluded because $\tau_\phi > \tau_{\text{BBN}}$. The regions above the red lines are excluded by Higgs invisible decay bounds.

partial widths for Higgs decays into ϕ and X_D pairs are

$$\Gamma_{h \rightarrow \phi\phi} = \frac{\lambda_{H\Phi}^2 v_h^2}{8\pi M_h} \sqrt{1 - \frac{4M_\phi^2}{M_h^2}}, \quad (6.3)$$

$$\Gamma_{h \rightarrow X_D X_D} = \frac{g_D^2 M_h^3 \sin^2 \theta}{8\pi M_{X_D}^2} \sqrt{1 - \frac{4M_{X_D}^2}{M_h^2}} \left(1 - \frac{4M_{X_D}^2}{M_h^2} + \frac{12M_{X_D}^4}{M_h^4} \right), \quad (6.4)$$

where $\lambda_{H\Phi}$ is the Higgs–portal coupling defined in Eq. (A.7).

In Fig. 5, we show the combined BBN and Higgs invisible decay constraints in the $\sin \theta$ - M_ϕ plane. The gray shaded region corresponds to $\tau_\phi > \tau_{\text{BBN}} = 1$ s and is therefore excluded by BBN. The red curves represent the Higgs invisible decay bounds for the four benchmark points in Table 1. For each benchmark, we fix g_D and M_{X_D} to their benchmark values and vary $\{M_\phi, \sin \theta\}$, such that the region below each red line satisfies $\mathcal{Br}(h \rightarrow \text{inv}) \leq 0.145$, while the region above is excluded. The values of M_ϕ corresponding to $BP1$, $BP2$, $BP3$, and $BP4$ are indicated by black solid, black dashed, black dotted, and black dashed-dotted vertical lines, respectively. It is evident that $BP1$ is ruled out by the Higgs invisible decay constraint, whereas $BP2$, $BP3$, and $BP4$ remain consistent with both BBN and Higgs invisible decay limits.

7 Gravitational wave from first-order phase transition

Having established the viability of our benchmark points against various constraints, we now turn to the gravitational wave signals generated by the dark sector phase transition. The stochastic gravitational wave background arising from a strong first-order phase transition is shaped by contributions from bubble collisions, sound waves in the plasma, and magnetohydrodynamic turbulence, as detailed in Appendix D. Here, we compute the GW spectrum for the four benchmark points listed in Table 1 and compare it against the projected sensitivities of existing and planned detectors.

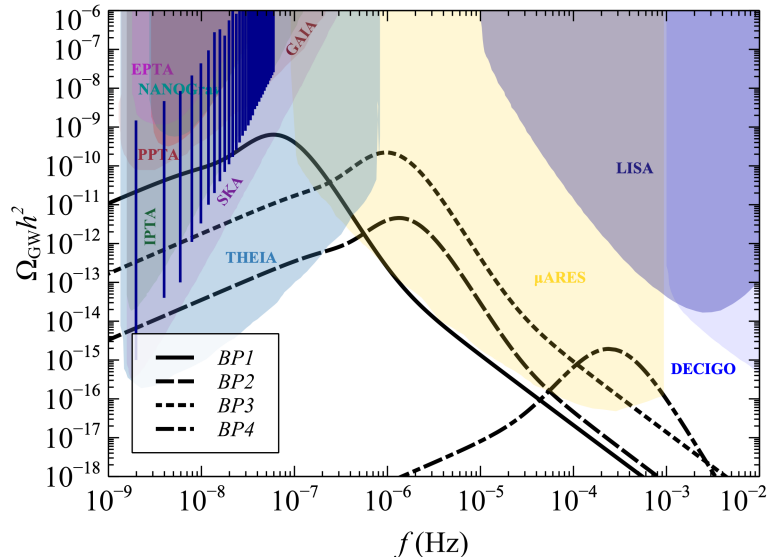


Figure 6: Gravitational wave spectrum for the four benchmark points listed in Table 1. The colored shaded regions indicate the projected sensitivities of different gravitational wave detectors.

In Fig. 6, we display the amplitude of the gravitational waves ($\Omega_{\text{GW}} h^2$) as a function of frequency f for each benchmark point. Sensitivities from NANOGRAV [44, 45], EPTA [46], PPTA [47], IPTA [48], SKA [49], LISA [50], THEIA [51], GAIA [51], DECIGO [52], and μ ARES [53] are shown with colored shaded regions in the same plot. The blue vertical lines represent the range of the GW spectrum indicated by the NANOGRAV results. For BP_1 , BP_2 , and BP_3 , the MeV-scale DM masses correspond to nucleation temperatures T_n also in the MeV range (cf. Table 1), placing their GW signals within reach of nHz gravitational wave experiments, including pulsar timing array (PTA) experiments, SKA, μ ARES, and astrometric observatories like THEIA. Remarkably, these spectra also overlap with the frequency and amplitude range preferred by the NANOGRAV signal [44], offering a potential explanation for this intriguing excess within our framework. For BP_4 , the GeV-scale DM mass leads to a nucleation temperature $T_n \sim 3$ GeV, shifting the peak frequency into the sensitivity range of μ ARES.

A distinctive feature of this scenario is the strong correlation between the DM mass M_χ and the nucleation temperature T_n of the phase transition. This connection arises naturally from the forbidden DM mechanism: obtaining the correct relic abundance requires the mass splitting Δ to remain $\mathcal{O}(1)$, which, in turn, demands that the final-state masses M_{X_D} and

M_ϕ scale proportionally with M_χ . Since $M_{X_D} = g_D v_\phi$ and $M_\phi = \sqrt{2\lambda_\Phi} v_\phi$, this necessitates a larger scalar vev v_ϕ for heavier DM, elevating the entire phase transition scale. Consequently, both the critical temperature T_c and nucleation temperature T_n increase monotonically with M_χ , as evident from the benchmark points in Table 1. This robust model prediction that heavier forbidden DM is accompanied by higher-scale phase transitions and correspondingly higher-frequency GW signals provides a powerful consistency check for the scenario and a clear target for near-future GW observations.

8 Conclusions

We have presented a minimal $U(1)_D$ gauge extension of the Standard Model featuring a Dirac fermion dark matter candidate χ and a complex singlet scalar Φ . By assigning the appropriate $U(1)_D$ charge to χ , its relic abundance is determined through the forbidden annihilation channel $\bar{\chi}\chi \rightarrow X_D\phi$, where X_D is the dark gauge boson and ϕ the physical scalar. The spontaneous breaking of the $U(1)_D$ symmetry serves a dual purpose: it generates masses for both X_D and ϕ , rendering the annihilation kinematically forbidden at late times, and simultaneously triggers a strong first-order phase transition in the dark sector.

This FOPT produces a stochastic gravitational wave background spanning the nHz to mHz frequency range, placing the signal within reach of existing pulsar timing arrays (NANOGrav, EPTA, PPTA, IPTA) and future detectors including SKA, THEIA, μ ARES, LISA, and DECIGO. Crucially, the $U(1)_D$ symmetry breaking proves indispensable for the viability of the scenario: in its absence, X_D and ϕ would remain massless, leading to unsuppressed annihilations that severely deplete the DM relic abundance for the couplings required for experimental accessibility.

The parameters governing the FOPT, *i.e.* the dark gauge coupling g_D , scalar quartic λ_ϕ , and vev v_ϕ , are strongly linked to the DM phenomenology. In particular, we uncover a robust correlation between the DM mass M_χ and the nucleation temperature T_n : heavier DM necessitates a higher phase-transition scale to maintain the appropriate mass splitting Δ for the forbidden mechanism, shifting the GW peak frequency accordingly. This model prediction offers a powerful consistency check, connecting the microscopic properties of DM to distinct gravitational wave signatures.

Due to the exponential suppression of late-time annihilations inherent to the forbidden channel, our scenario comfortably evades stringent constraints from CMB observations and indirect detection experiments. The benchmark points satisfying the observed relic density also survive existing direct detection and other phenomenological bounds while remaining testable by near future low threshold experiments. Taken together, this framework demonstrates that a strong connection between DM freeze-out and early Universe phase transitions can simultaneously address the relic density puzzle, explain potential gravitational wave signals, and yield rich, mutually reinforcing experimental signatures across multiple frontiers.

Acknowledgments

P.K.P. would like to acknowledge the Ministry of Education, Government of India, for providing financial support for his research via the Prime Minister's Research Fellowship (PMRF) scheme. Parts of this work were developed through discussions among the authors at the *Phoenix 2025* conference, and we thank the organizers for providing a stimulating environment. S.M. acknowledges support from the IIT Goa Startup Grant [2025/SG/SM/057].

A SM Higgs and Φ mixing

The scalar potential of the model containing the singlet scalar Φ and the SM Higgs doublet H is given by

$$V(H, \Phi) = -\mu_\Phi^2 \Phi^2 - \mu_H^2 (H^\dagger H) + \lambda_H (H^\dagger H)^2 + \lambda_\Phi \Phi^4 + \lambda_{H\Phi} (H^\dagger H) \Phi^2 \quad (\text{A.1})$$

Parameterizing the scalars H and Φ as

$$H = \frac{1}{\sqrt{2}} \begin{pmatrix} 0 \\ v_h + h \end{pmatrix}, \quad \Phi = \frac{\phi + v_\phi}{\sqrt{2}} \quad (\text{A.2})$$

where the vevs are estimated to be

$$v_h = \sqrt{\frac{2\mu_H^2 - \lambda_{H\Phi} v_\phi^2}{2\lambda_H}}, \quad v_\phi = \sqrt{\frac{2\mu_\Phi^2 - \lambda_{H\Phi} v_h^2}{2\lambda_\Phi}}.$$

The mass-squared matrix spanning the h and ϕ is given by

$$M_{h\phi}^2 = \begin{pmatrix} 2\lambda_H v_h^2 & \lambda_{H\Phi} v_h v_\phi \\ \lambda_{H\Phi} v_h v_\phi & 2\lambda_\Phi v_\phi^2 \end{pmatrix}. \quad (\text{A.3})$$

Diagonalizing the above mass matrix, we get the mass eigenstates h_1 with mass $M_{h_1} = 125$ GeV and h_2 with mass M_{h_2} . The $h - \phi$ mixing angle is then given by

$$\tan 2\theta \sim \frac{\lambda_{H\Phi} v_h v_\phi}{\lambda_H v_h^2 - \lambda_\Phi v_\phi^2}. \quad (\text{A.4})$$

The scalar couplings can be expressed in terms of the scalar masses and mixing angle as

$$\lambda_H = \frac{\cos \theta^2 M_{h_1}^2 + \sin \theta^2 M_{h_2}^2}{2v_h^2} \quad (\text{A.5})$$

$$\lambda_\Phi = \frac{\cos \theta^2 M_{h_2}^2 + \sin \theta^2 M_{h_1}^2}{2v_\phi^2} \quad (\text{A.6})$$

$$\lambda_{H\Phi} = \cos \theta \sin \theta \frac{M_{h_1}^2 - M_{h_2}^2}{v_h v_\phi} \quad (\text{A.7})$$

B DM annihilation and scattering cross-sections

We used `CalcHEP` [54] for computing the cross-sections after implementing the model in `Lanhep` [55]. The thermally averaged cross-section for the forbidden channel, $\chi\bar{\chi} \rightarrow X_D\phi$ can be written as

$$\langle\sigma v\rangle_{\chi\bar{\chi} \rightarrow X_D\phi} = \frac{n_{X_D}^{\text{eq}} n_\phi^{\text{eq}}}{(n_\chi^{\text{eq}})^2} \langle\sigma v\rangle_{X_D\phi \rightarrow \chi\bar{\chi}}, \quad (\text{B.1})$$

where the thermally averaged cross-section is given as

$$\begin{aligned} \langle\sigma v\rangle_{12 \rightarrow 34} = & \frac{T}{8m_1^2 m_2^2 K_2(\frac{m_1}{T}) K_2(\frac{m_2}{T})} \int_{\max[(m_1+m_2)^2, (m_3+m_4)^2]}^{\infty} ds \sigma(s) \sqrt{s} K_1\left(\frac{\sqrt{s}}{T}\right) \\ & \times (s - \max[(m_1+m_2)^2, (m_3+m_4)^2]). \end{aligned} \quad (\text{B.2})$$

C Details of first-order phase transition

The finite temperature effective potential is given as

$$V_{\text{eff}}(\phi, T) = V_{\text{tree}}(\phi) + V_{\text{CW}}(\phi) + V_{\text{ct}}(\phi) + V_T(\phi, T) + V_{\text{daisy}}(\phi, T). \quad (\text{C.1})$$

The tree-level part of the potential is given as

$$V_{\text{tree}} = -\frac{1}{2}\lambda_{\Phi}v_{\phi}^2\phi^2 + \frac{1}{4}\lambda_{\Phi}\phi^4. \quad (\text{C.2})$$

The one-loop Coleman-Weinberg zero temperature contribution in $\overline{\text{MS}}$ renormalization scheme is given as

$$V_{\text{CW}} = \frac{1}{64\pi^2}m_{\phi}^4(\phi)\left(\log\left(\frac{m_{\phi}^2(\phi)}{\mu_R^2}\right) - \frac{3}{2}\right) + \frac{3}{64\pi^2}m_{X_D}^4(\phi)\left(\log\left(\frac{m_{X_D}^2(\phi)}{\mu_R^2}\right) - \frac{5}{6}\right), \quad (\text{C.3})$$

where the field-dependent masses are given as

$$m_{\phi}(\phi) = \sqrt{-\lambda_{\Phi}v^2 + 3\lambda_{\Phi}\phi^2}; M_{Z_D}(\phi) = g_D\phi. \quad (\text{C.4})$$

The renormalization scale is fixed at $\mu_R \equiv v_{\phi}$. The counter term is

$$V_{\text{ct}} = -\frac{\delta\mu_{\Phi}^2}{2}\phi^2 + \frac{\delta\lambda_{\Phi}}{4}\phi^4, \quad (\text{C.5})$$

which is derived by solving

$$\frac{\partial(V_{\text{CW}} + V_{\text{ct}})}{\partial\phi}\bigg|_{\phi=v_{\phi}} = 0, \quad \frac{\partial^2(V_{\text{CW}} + V_{\text{ct}})}{\partial\phi^2}\bigg|_{\phi=v_{\phi}} = 0. \quad (\text{C.6})$$

The finite temperature contribution is given as

$$V_T = \frac{T^4}{2\pi^2}J_B\left(\frac{m_{\phi}(\phi)}{T}\right) + \frac{T^4}{2\pi^2}J_B\left(\frac{m_{\eta}(\phi)}{T}\right) + 3\frac{T^4}{2\pi^2}J_B\left(\frac{m_{X_D}(\phi)}{T}\right), \quad (\text{C.7})$$

where, $m_{\eta}(\phi) = \sqrt{-\lambda_{\Phi}v^2 + \lambda_{\eta}\phi^2}$ and

$$J_B(y) = \int_0^{\infty}x^2\log(1 - e^{-\sqrt{x^2+y^2}}) \quad (\text{C.8})$$

The daisy contribution is

$$V_{\text{daisy}} = -\frac{g_D^3 T}{12\pi}\left(\left(\phi^2 + T^2\right)^{3/2} - \phi^3\right). \quad (\text{C.9})$$

The bubble nucleation rate per unit volume at a finite temperature is given by

$$\Gamma(T) \simeq \left(\frac{S_3(T)}{2\pi T}\right)^{3/2}T^4 e^{-\frac{S_3(T)}{T}}, \quad (\text{C.10})$$

where S_3 is the three-dimensional Euclidean action given as

$$S_3(T) = \int d^3r\left[\frac{1}{2}\left(\frac{d\phi}{dr}\right)^2 + V_{\text{eff}}(\phi, T)\right], \quad (\text{C.11})$$

which is calculated by solving

$$\frac{d^2\phi}{dr^2} + \frac{2}{r} \frac{d\phi}{dr} - \frac{dV_{\text{eff}}(\phi, T)}{d\phi} = 0, \quad (\text{C.12})$$

with the following boundary conditions

$$\left. \frac{d\phi}{dr} \right|_{r=0} = 0, \quad \phi(\infty) = \phi_{\text{false}}. \quad (\text{C.13})$$

The nucleation process begins when the bubble nucleation rate becomes comparable to the Hubble expansion rate, which is described by

$$\Gamma(T_n) \approx \mathcal{H}(T_n)^4, \quad (\text{C.14})$$

where T_n is the nucleation temperature.

D Gravitational waves

(i) Bubble collision:

The peak frequency and the amplitude of the GWs generated by the bubble collision are given by

$$f_{\text{peak}}^{\text{col}} = 1.65 \times 10^{-5} \text{ (Hz)} \left(\frac{g_*(T_n)}{100} \right)^{1/6} \left(\frac{T_n}{0.1 \text{ TeV}} \right) \frac{0.64}{2\pi} \left(\frac{\beta(T_n)}{\mathcal{H}(T_n)} \right), \quad (\text{D.1})$$

$$\Omega_{\text{col}} h^2 = 1.65 \times 10^{-5} \left(\frac{100}{g_*(T_n)} \right)^{1/3} \left(\frac{\mathcal{H}(T_n)}{\beta(T_n)} \right) \left(\frac{\kappa_\phi(T_n) \alpha(T_n)}{1 + \alpha(T_n)} \right)^2 \frac{A(a+b)^c}{\left(b \left(\frac{f}{f_{\text{peak}}^{\text{col}}} \right)^{-a/c} + a \left(\frac{f}{f_{\text{peak}}^{\text{col}}} \right)^{b/c} \right)^c \right)}, \quad (\text{D.2})$$

with the efficiency factor

$$\kappa_\phi = \frac{1}{1 + 0.715\alpha(T_n)} \left(0.715\alpha(T_n) + \frac{4}{27} \sqrt{\frac{3\alpha(T_n)}{2}} \right), \quad (\text{D.3})$$

and $a = 1.03, b = 1.84, c = 1.45, A = 5.93 \times 10^{-2}$ [33, 56, 57].

(ii) Sound waves:

The peak frequency and the amplitude of the GWs generated by the sound waves are expressed by [33]

$$f_{\text{peak}}^{\text{sw}} = 8.9 \times 10^{-6} \text{ (Hz)} \left(\frac{g_*(T_n)}{100} \right)^{1/6} \left(\frac{1}{v_w} \right) \left(\frac{T_n}{0.1 \text{ TeV}} \right) \left(\frac{z_p}{10} \right) \left(\frac{\beta(T_n)}{\mathcal{H}(T_n)} \right) \quad (\text{D.4})$$

where the wall velocity $v_w \sim 1$, and $z_p \sim 10$.

$$\Omega_{\text{sw}} h^2 = 2.59 \times 10^{-6} \left(\frac{100}{g_*(T_n)} \right)^{1/3} \left(\frac{\mathcal{H}(T_n)}{\beta(T_n)} \right) v_w \Upsilon(T_n) \left(\frac{\kappa_{\text{sw}}(T_n) \alpha(T_n)}{1 + \alpha(T_n)} \right)^2 \frac{7^{3.5} \left(\frac{f}{f_{\text{peak}}^{\text{sw}}(T_n)} \right)^3}{\left(4 + 3 \left(\frac{f}{f_{\text{peak}}^{\text{col}}(T_n)} \right)^2 \right)^{3.5}}. \quad (\text{D.5})$$

The efficiency factor is [58]

$$\kappa_{\text{sw}} = \frac{\alpha(T_n)}{0.73 + 0.083 \sqrt{\alpha(T_n)} + \alpha(T_n)} \quad (\text{D.6})$$

The suppression factor is given as

$$\Upsilon = 1 - \frac{1}{\sqrt{1 + 2\tau_{\text{sw}}(T_n) \mathcal{H}(T_n)}}, \quad (\text{D.7})$$

where the lifetime of the sound wave is given as [59]

$$\tau_{\text{sw}} = \frac{R_*(T_n)}{U_f(T_n)}, \quad (\text{D.8})$$

where mean bubble separation is given by

$$R_* = \frac{(8\pi)^{1/3} v_w}{\beta(T_n)}, \quad (\text{D.9})$$

and the rms fluid velocity is given as

$$U_f = \sqrt{\frac{3\kappa_{\text{sw}}(T_n) \alpha(T_n)}{4(1 + \alpha(T_n))}}. \quad (\text{D.10})$$

(iii) Turbulence:

The peak frequency and the amplitude of the GWs generated by the turbulence are expressed by [33, 57, 60]

$$f_{\text{peak}}^{\text{turb}} = 2.7 \times 10^{-5} \text{ (Hz)} \left(\frac{g_*(T_n)}{100} \right)^{1/6} \left(\frac{1}{v_w} \right) \left(\frac{T_n}{0.1 \text{ TeV}} \right) \left(\frac{\beta(T_n)}{\mathcal{H}(T_n)} \right), \quad (\text{D.11})$$

$$\Omega_{\text{turb}} h^2 = 3.35 \times 10^{-4} \left(\frac{100}{g_*(T_n)} \right)^{1/3} \left(\frac{\mathcal{H}(T_n)}{\beta(T_n)} \right) \left(\frac{\kappa_{\text{turb}}(T_n) \alpha(T_n)}{1 + \alpha(T_n)} \right)^2 v_w \frac{\left(\frac{f}{f_{\text{peak}}^{\text{sw}}(T_n)} \right)^3}{\left(1 + \left(\frac{f}{f_{\text{peak}}^{\text{col}}(T_n)} \right)^2 \right)^{3.6} \left(1 + \frac{8\pi f}{h_*(T_n)} \right)}, \quad (\text{D.12})$$

where the efficiency factor is $\kappa_{\text{turb}} = 0.1 \kappa_{\text{sw}}$ [60], and the inverse of the Hubble time at the epoch of GW production, red-shifted to today, is expressed as:

$$h_* = 1.65 \times 10^{-5} \text{ (Hz)} \left(\frac{g_*(T_n)}{100} \right)^{1/6} \left(\frac{T_n}{0.1 \text{ TeV}} \right) \quad (\text{D.13})$$

References

- [1] F. Zwicky, *Die Rotverschiebung von extragalaktischen Nebeln*, *Helv. Phys. Acta* **6** (1933) 110.
- [2] V.C. Rubin and W.K. Ford, Jr., *Rotation of the Andromeda Nebula from a Spectroscopic Survey of Emission Regions*, *Astrophys. J.* **159** (1970) 379.
- [3] D. Clowe, M. Bradac, A.H. Gonzalez, M. Markevitch, S.W. Randall, C. Jones et al., *A direct empirical proof of the existence of dark matter*, *Astrophys. J. Lett.* **648** (2006) L109 [[astro-ph/0608407](#)].
- [4] PLANCK collaboration, *Planck 2018 results. VI. Cosmological parameters*, *Astron. Astrophys.* **641** (2020) A6 [[1807.06209](#)].
- [5] PARTICLE DATA GROUP collaboration, *Review of Particle Physics*, *PTEP* **2020** (2020) 083C01.
- [6] G. Arcadi, D. Cabo-Almeida, M. Dutra, P. Ghosh, M. Lindner, Y. Mambrini et al., *The Waning of the WIMP: Endgame?*, *Eur. Phys. J. C* **85** (2025) 152 [[2403.15860](#)].
- [7] G. Arcadi, M. Dutra, P. Ghosh, M. Lindner, Y. Mambrini, M. Pierre et al., *The waning of the WIMP? A review of models, searches, and constraints*, *Eur. Phys. J. C* **78** (2018) 203 [[1703.07364](#)].
- [8] S. Balan et al., *Resonant or asymmetric: the status of sub-GeV dark matter*, *JCAP* **01** (2025) 053 [[2405.17548](#)].
- [9] A. Cheek, P. Figueroa, G. Herrera and I.M. Shoemaker, *Sub-GeV Dark Matter Under Pressure from Direct Detection*, [2507.15956](#).
- [10] G. Krnjaic, *Testing Thermal-Relic Dark Matter with a Dark Photon Mediator*, [2505.04626](#).
- [11] B. Dutta, S. Ghosh and J. Kumar, *A sub-GeV dark matter model*, *Phys. Rev. D* **100** (2019) 075028 [[1905.02692](#)].
- [12] R. Essig, T. Volansky and T.-T. Yu, *New Constraints and Prospects for sub-GeV Dark Matter Scattering off Electrons in Xenon*, *Phys. Rev. D* **96** (2017) 043017 [[1703.00910](#)].
- [13] K. Bondarenko, A. Boyarsky, T. Bringmann, M. Hufnagel, K. Schmidt-Hoberg and A. Sokolenko, *Direct detection and complementary constraints for sub-GeV dark matter*, *JHEP* **03** (2020) 118 [[1909.08632](#)].
- [14] A. Adhikary, D. Borah, S. Mahapatra, I. Saha, N. Sahu and V.S. Thounaojam, *New realisation of light thermal dark matter with enhanced detection prospects*, *JCAP* **12** (2024) 043 [[2405.17564](#)].
- [15] D. Borah, P. Das, S. Mahapatra and N. Sahu, *Light thermal dark matter via type-I seesaw portal*, *JHEP* **08** (2025) 023 [[2401.01639](#)].
- [16] D. Borah, S. Mahapatra, N. Sahu and V.S. Thounaojam, *Light thermal dark matter models in the light of DAMIC-M 2025 constraints*, [2509.16319](#).
- [17] E. Ma, P.K. Paul and N. Sahu, *Lepton parity dark matter and naturally unstable domain walls*, *Phys. Rev. D* **112** (2025) 095020 [[2508.02642](#)].
- [18] E. Ma, P.K. Paul and N. Sahu, *Cosmological Probes of Lepton Parity Freeze-in Dark Matter: ΔN_{eff} & Gravitational Waves*, [2511.21634](#).
- [19] XENON collaboration, *Light Dark Matter Search with Ionization Signals in XENON1T*, *Phys. Rev. Lett.* **123** (2019) 251801 [[1907.11485](#)].
- [20] CRESST collaboration, *First results from the CRESST-III low-mass dark matter program*, *Phys. Rev. D* **100** (2019) 102002 [[1904.00498](#)].
- [21] XENON collaboration, *Search for Light Dark Matter in Low-Energy Ionization Signals from XENONnT*, *Phys. Rev. Lett.* **134** (2025) 161004 [[2411.15289](#)].

[22] PANDAX-II collaboration, *Search for Light Dark Matter-Electron Scatterings in the PandaX-II Experiment*, *Phys. Rev. Lett.* **126** (2021) 211803 [[2101.07479](#)].

[23] PANDAX collaboration, *Search for Light Dark Matter with Ionization Signals in the PandaX-4T Experiment*, *Phys. Rev. Lett.* **130** (2023) 261001 [[2212.10067](#)].

[24] SENSEI collaboration, *SENSEI: Direct-Detection Results on sub-GeV Dark Matter from a New Skipper-CCD*, *Phys. Rev. Lett.* **125** (2020) 171802 [[2004.11378](#)].

[25] SUPERCDMS collaboration, *Light dark matter constraints from SuperCDMS HVeV detectors operated underground with an anticoincidence event selection*, *Phys. Rev. D* **111** (2025) 012006 [[2407.08085](#)].

[26] DAMIC-M collaboration, *Probing Benchmark Models of Hidden-Sector Dark Matter with DAMIC-M*, [2503.14617](#).

[27] T.R. Slatyer, *Indirect dark matter signatures in the cosmic dark ages. I. Generalizing the bound on s-wave dark matter annihilation from Planck results*, *Phys. Rev. D* **93** (2016) 023527 [[1506.03811](#)].

[28] A. McDaniel, M. Ajello, C.M. Karwin, M. Di Mauro, A. Drlica-Wagner and M.A. Sánchez-Conde, *Legacy analysis of dark matter annihilation from the Milky Way dwarf spheroidal galaxies with 14 years of Fermi-LAT data*, *Phys. Rev. D* **109** (2024) 063024 [[2311.04982](#)].

[29] A. Cuoco, M. Krämer and M. Korsmeier, *Novel Dark Matter Constraints from Antiprotons in Light of AMS-02*, *Phys. Rev. Lett.* **118** (2017) 191102 [[1610.03071](#)].

[30] R.T. D’Agnolo and J.T. Ruderman, *Light Dark Matter from Forbidden Channels*, *Phys. Rev. Lett.* **115** (2015) 061301 [[1505.07107](#)].

[31] R.T. D’Agnolo, D. Liu, J.T. Ruderman and P.-J. Wang, *Forbidden dark matter annihilations into Standard Model particles*, *JHEP* **06** (2021) 103 [[2012.11766](#)].

[32] M.B. Hindmarsh, M. Lüben, J. Lumma and M. Pauly, *Phase transitions in the early universe*, *SciPost Phys. Lect. Notes* **24** (2021) 1 [[2008.09136](#)].

[33] P. Athron, C. Balázs, A. Fowlie, L. Morris and L. Wu, *Cosmological phase transitions: From perturbative particle physics to gravitational waves*, *Prog. Part. Nucl. Phys.* **135** (2024) 104094 [[2305.02357](#)].

[34] S. Mahapatra, P.K. Paul, N. Sahu and P. Shukla, *Verifiable type-III seesaw and dark matter in a gauged $U(1)_{B-L}$ symmetric model*, [2504.00109](#).

[35] E. Ma, P.K. Paul and N. Sahu, *Naturally small Dirac neutrino mass and $B - L$ dark matter*, [2601.05926](#).

[36] GLOBAL ARGON DARK MATTER collaboration, *Sensitivity projections for a dual-phase argon TPC optimized for light dark matter searches through the ionization channel*, *Phys. Rev. D* **107** (2023) 112006 [[2209.01177](#)].

[37] DARKSIDE collaboration, *Search for Dark Matter Particle Interactions with Electron Final States with DarkSide-50*, *Phys. Rev. Lett.* **130** (2023) 101002 [[2207.11968](#)].

[38] DARKSIDE-50 collaboration, *Search for low-mass dark matter WIMPs with 12 ton-day exposure of DarkSide-50*, *Phys. Rev. D* **107** (2023) 063001 [[2207.11966](#)].

[39] SUPERCDMS collaboration, *Projected Sensitivity of the SuperCDMS SNOLAB experiment*, *Phys. Rev. D* **95** (2017) 082002 [[1610.00006](#)].

[40] D. Banerjee et al., *Dark matter search in missing energy events with NA64*, *Phys. Rev. Lett.* **123** (2019) 121801 [[1906.00176](#)].

[41] BABAR collaboration, *Search for a Dark Photon in e^+e^- Collisions at BaBar*, *Phys. Rev. Lett.* **113** (2014) 201801 [[1406.2980](#)].

[42] J.H. Chang, R. Essig and S.D. McDermott, *Revisiting Supernova 1987A Constraints on Dark Photons*, *JHEP* **01** (2017) 107 [[1611.03864](#)].

[43] ATLAS collaboration, *Search for invisible Higgs-boson decays in events with vector-boson fusion signatures using 139 fb^{-1} of proton-proton data recorded by the ATLAS experiment*, *JHEP* **08** (2022) 104 [[2202.07953](#)].

[44] NANOGrav collaboration, *The NANOGrav 15 yr Data Set: Evidence for a Gravitational-wave Background*, *Astrophys. J. Lett.* **951** (2023) L8 [[2306.16213](#)].

[45] NANOGrav collaboration, *The NANOGrav 15 yr Data Set: Search for Signals from New Physics*, *Astrophys. J. Lett.* **951** (2023) L11 [[2306.16219](#)].

[46] EPTA, INPTA: collaboration, *The second data release from the European Pulsar Timing Array - III. Search for gravitational wave signals*, *Astron. Astrophys.* **678** (2023) A50 [[2306.16214](#)].

[47] D.J. Reardon et al., *Search for an Isotropic Gravitational-wave Background with the Parkes Pulsar Timing Array*, *Astrophys. J. Lett.* **951** (2023) L6 [[2306.16215](#)].

[48] G. Hobbs et al., *The international pulsar timing array project: using pulsars as a gravitational wave detector*, *Class. Quant. Grav.* **27** (2010) 084013 [[0911.5206](#)].

[49] A. Weltman et al., *Fundamental physics with the Square Kilometre Array*, *Publ. Astron. Soc. Austral.* **37** (2020) e002 [[1810.02680](#)].

[50] LISA collaboration, *Laser Interferometer Space Antenna*, [1702.00786](#).

[51] J. Garcia-Bellido, H. Murayama and G. White, *Exploring the early Universe with Gaia and Theia*, *JCAP* **12** (2021) 023 [[2104.04778](#)].

[52] E.G. Adelberger, N.A. Collins and C.D. Hoyle, *Analytic expressions for gravitational inner multipole moments of elementary solids and for the force between two rectangular solids*, *Class. Quant. Grav.* **23** (2006) 125 [[gr-qc/0512055](#)].

[53] A. Sesana et al., *Unveiling the gravitational universe at $\mu\text{-Hz}$ frequencies*, *Exper. Astron.* **51** (2021) 1333 [[1908.11391](#)].

[54] A. Belyaev, N.D. Christensen and A. Pukhov, *CalcHEP 3.4 for collider physics within and beyond the Standard Model*, *Comput. Phys. Commun.* **184** (2013) 1729 [[1207.6082](#)].

[55] A. Semenov, *LanHEP — A package for automatic generation of Feynman rules from the Lagrangian. Version 3.2*, *Comput. Phys. Commun.* **201** (2016) 167 [[1412.5016](#)].

[56] M. Lewicki and V. Vaskonen, *Gravitational waves from bubble collisions and fluid motion in strongly supercooled phase transitions*, *Eur. Phys. J. C* **83** (2023) 109 [[2208.11697](#)].

[57] LISA COSMOLOGY WORKING GROUP collaboration, *Gravitational waves from first-order phase transitions in LISA: reconstruction pipeline and physics interpretation*, *JCAP* **10** (2024) 020 [[2403.03723](#)].

[58] J.R. Espinosa, T. Konstandin, J.M. No and G. Servant, *Energy Budget of Cosmological First-order Phase Transitions*, *JCAP* **06** (2010) 028 [[1004.4187](#)].

[59] H.-K. Guo, K. Sinha, D. Vagie and G. White, *Phase Transitions in an Expanding Universe: Stochastic Gravitational Waves in Standard and Non-Standard Histories*, *JCAP* **01** (2021) 001 [[2007.08537](#)].

[60] C. Caprini et al., *Science with the space-based interferometer eLISA. II: Gravitational waves from cosmological phase transitions*, *JCAP* **04** (2016) 001 [[1512.06239](#)].